The effect of distortion models on characterisation of real defects using ultrasonic arrays

Long Bai[a,*], Alexander Velichko[a], Adam T. Clare[b], Paul Dryburgh[b,c], Don Pieris[b,c], Bruce W. Drinkwater[a]

[a] *Department of Mechanical Engineering, University of Bristol, Queens Building, University Walk, Bristol BS8 1TR, UK*
[b] *Advanced Component Engineering Laboratory, University of Nottingham, Jubilee Campus, Nottingham NG8 1BB, UK*
[c] *Optics and Photonics Group, University of Nottingham, University Park, Nottingham NG7 2RD, UK*

Abstract

Characterisation of real defects is one of the main challenges in ultrasonic non-destructive testing (NDT), especially for small defects having irregular shapes. Traditional methods such as ultrasonic array imaging are limited by the image resolution, and in this paper, we consider using the scattering matrix which is extractable from the full matrix of transmit-receive array data. We describe a procedure in which the experimental measurements are used to perform characterisation and reveal the associated uncertainties. Moreover, we explore performance of this characterisation procedure and propose a robust defect characterisation approach. The performance of the proposed approach is studied experimentally, and the sizing errors are small (within 0.09λ or 0.23mm for fatigue cracks at 2.5 MHz, and within 0.38λ or 0.24mm for volumetric defects in an additive manufactured specimen at 10 MHz). In addition, reliable estimation of defect angle/width is achieved.

Keywords: Ultrasonic array, Defect characterisation, Scattering matrix, Distortion model

*Corresponding author
Email addresses: bailong_hust@foxmail.com (Long Bai), a.velichko@bristol.ac.uk (Alexander Velichko), adam.clare@nottingham.ac.uk (Adam T. Clare), paul.dryburgh@nottingham.ac.uk (Paul Dryburgh), eexdmp@nottingham.ac.uk (Don Pieris), b.drinkwater@bristol.ac.uk (Bruce W. Drinkwater)

1. Introduction

Ultrasonic inspection is an important technique in non-destructive testing (NDT) [1] and its use can be found in a range of safety critical applications, including nuclear [2], railway [3], petroleum [4, 5], and aerospace industries [6]. Besides facilitating detection of defects which can cause catastrophic failure of a structure, an ideal inspection technique should also provide the capability to characterise defects after they are detected. This enables an operator to compare different defects in terms of their impacts on structural integrity based on an understanding of the defect size and type and hence, can potentially reduce the number of unnecessary replacements of components [7].

Ultrasonic arrays are increasingly used in NDT thanks to their flexibility and the availability of array controller systems with which one can specify time delays of individual array elements [8]. One possible data acquisition scheme for ultrasonic arrays is the full matrix capture (FMC) [9]. The FMC dataset contains time-domain signals corresponding to all transmitter-receiver pairs of an array, and imaging can be performed by post-processing the FMC data [10]. With the help of advanced imaging algorithms such as the total focusing method (TFM) [9] and plane wave imaging [11], the capability of ultrasonic inspection has been improved significantly. For example, Shahjahan *et al.* used the decomposition of the time reversal operator (DORT [12]) algorithm to filter the FMC data for detection of 2mm side drilled holes in a highly scattering medium [13]. Lin *et al.* proposed a model-based approach to calculate the time delays used for TFM imaging in multidirectional CFRP laminates for improved detection and sizing of delamination [14]. The 6dB drop approach [15] is widely used in ultrasonic NDT as a means to sizing defects and is included in various international standards such as BS EN ISO 16827 [16] and ASTM E2700-14 [17]. The defect size is determined by the 6dB drop approach as the distance over which the A-scan amplitude drops by one half (*i.e.* 6 dB) from the maximum value. Besides A-scan signals measured from single element transducers, the 6dB drop

approach can also be applied to images formed using an ultrasonic array. For example, Zhang *et al.* used a rectangular box to cover all image pixels within −6 dB from the identified peak value, and measured the size and angle of crack-like defects from the dimensions of such rectangular boxes [18]. However, defect type information is not considered in the 6 dB drop approach and its performance can become poor for defects having irregular shapes and/or unfavourable orientations [19]. In addition, the performance of image-based sizing depends on the imaging resolution and hence, is limited by diffraction.

In this paper, we focus our attention on characterisation of small defects (*i.e.* sizes comparable to the wavelength), and in particular, we aim to develop a robust defect characterisation procedure that is suitable for automated NDT. Besides sizing, accurate characterisation also requires the measurement of other critical parameters such as defect type, aspect ratio and orientation angle. Here, the scattering matrix [20], extractable from the FMC data, is used in an inversion scheme aimed at retrieving the defect parameters based on Bayes theorem [21]. In this paper, we define the "distortion" as the difference between the experimentally measured and idealised scattering matrices. The importance of the distortion model on the characterisation performance is demonstrated using experimental data measured from machined surface-breaking notches. We also extract experimental data from more realistic defects, including surface-breaking fatigue cracks [22] and volumetric defects in an additive manufactured (AM) Aluminium sample [23] built using the laser powder bed fusion (L-PBF) technique [24]. Besides the volumetric defects that were deliberately introduced, the AM sample also contains material discontinuities (*e.g.* low level porosity, inter layer delaminations, and small grains [25]) that can occur during the manufacturing process. These material discontinuities act as noise sources when performing measurements using ultrasound, and hence, add additional level of complexity to the characterisation problem. The optimal distortion model is difficult to determine in advance for these real defects, and we show that robust defect characterisation is still achievable by combining the results obtained with different distortion models.

2. Characterisation of small defects using the scattering matrix

2.1. Measurement configuration

To begin with, let us consider the machined surface-breaking notches in an Aluminium sample shown in Fig. 1(a). These notches were manufactured using electrical discharge machining (EDM) and have smooth surfaces, so they can be regarded as the idealised defects (*i.e.* surface scratches), as opposed to real defects which are covered in the next section. The shape of these notches is described by two parameters, width a and depth b (see Table 1 for parameter values of the manufactured notches). A 2.5 MHz, 64 element array with an element pitch of 0.5mm is used in experiments under the measurement configuration shown in Fig. 1(b). The TFM is applied to the measured FMC data of the defects and Figs. 2(a)-2(b) are imaging results of Notches 6 and 7 (a Gaussian filter having 100% bandwidth is applied to the time-domain signals in post-processing to reduce noise). Note that the ultrasonic wavelength is 2.5mm when the frequency is 2.5 MHz, and the maximum width and depth of the notches are 1.5 wavelengths. It can be seen that Notches 6 and 7 are indistinguishable from their TFM results and hence, the information provided by imaging is insufficient for characterisation of these small notches.

Table 1: Width a and depth b of Notches 1-8 shown in Fig. 1(a).

Notch	1	2	3	4	5	6	7	8
Width (a, mm)	1.25	1.25	2.5	2.5	2.5	3.75	3.75	3.75
Depth (b, mm)	1.25	2.5	1.25	2.5	3.75	1.25	2.5	3.75

The ultrasonic scattering matrix contains the far-field scattering coefficients of a defect and is known to contain all the defect information that can be measured from an experimental configuration [20, 21]. It can be extracted from an FMC dataset through a procedure (*e.g.* sub-array imaging [20] or inverse imaging approaches [26]) designed to suppress noise/interferences from nearby defects. We define the scattering matrix in a 2D scenario as

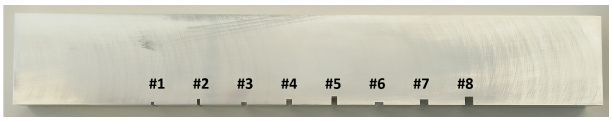

(a)

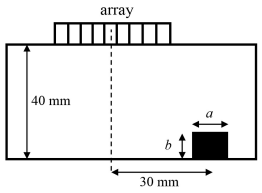

(b)

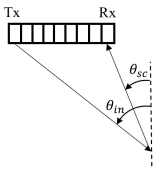

(c)

Figure 1: (a) An Aluminium test specimen containing 8 machined notches, (b) measurement configuration adopted in experiments, and (c) incident and scattering angle definitions for the transmitter element Tx and receiver element Rx of an array.

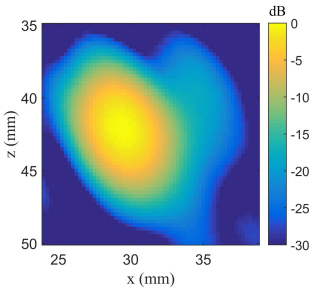

(a)

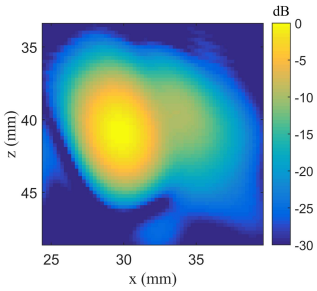

(b)

Figure 2: TFM results of (a) Notch 6 and (b) Notch 7, obtained at 2.5 MHz. Both images show a 15mm×15mm region including the defect.

$$\boldsymbol{s}(\theta_{\text{in}}, \theta_{\text{sc}}, \omega) = \frac{a_{\text{sc}}(\omega)}{a_{\text{in}}(\omega)} \sqrt{\frac{d_{\text{sc}}}{\lambda}} \exp\left(-\frac{i\omega d_{\text{sc}}}{c}\right). \tag{1}$$

In Eq. (1), θ_{in} and θ_{sc} denote the incident and scattering angles (see Fig. 1(c)), a_{in} and a_{sc} are amplitude of the plane incident wave and the scattered wave measured at a distance d_{sc} from the defect, $\omega = 2\pi f$ is the angular frequency, and c is the ultrasonic velocity (6300 m/s for Aluminium). Note that

matrices and vectors are denoted in this paper by bold upper- and lower-case letters, respectively, and we will use a vectorised version of the scattering matrix representation throughout this paper. Figures 3(a)-3(b) show the experimentally measured scattering matrices of Notches 6 and 7 and they are seen to be different, suggesting that scattering-matrix-based characterisation is possible. Note that when the probe is right above the small surface defects, the relatively weak defect signal is overlapped with strong backwall reflections, and in this case, it would be very difficult to size it. Using the configuration shown in Fig. 1(b), the defect signal is separated in time domain from backwall reflections, which facilitates extraction of the defect scattering matrix without interferences from the backwall. Phase part of the scattering matrix is not considered in this paper because phase measurements are very sensitive to localisation errors and have higher uncertainty than the amplitude [27].

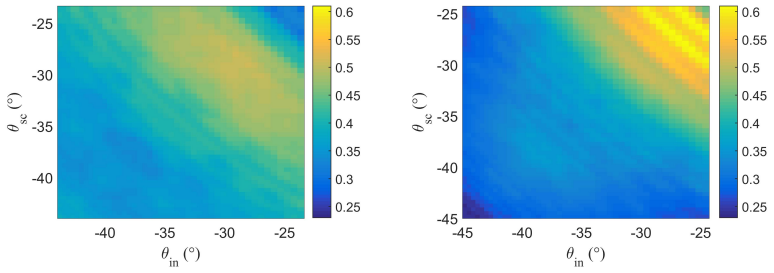

(a) (b)

Figure 3: Scattering matrices of (a) Notch 6 and (b) Notch 7.

2.2. Defect characterisation procedure

The defect characterisation problem can be formulated as calculating the probability $P(\boldsymbol{p}|\boldsymbol{s}_n)$, *i.e.*, the conditional probability of a defect parameter $\boldsymbol{p}$ given the measurement of a scattering matrix $\boldsymbol{s}_n$ [21]. The defect parameter $\boldsymbol{p}$ consists of the physical quantities that describe the geometry of a given type of defects, and we have $\boldsymbol{p} = [a, b]^T$ for surface-breaking notches. An experimentally measured scattering matrix $\boldsymbol{s}_n$ is often contaminated by noise from different

sources, and in this paper, we define distortion as the difference between the measurement $\boldsymbol{s}_n$ and idealised scattering matrices of reference scatterers. Following this, we have

$$\boldsymbol{s}_n = \boldsymbol{s}_p + \boldsymbol{n}_p, \tag{2}$$

where $\boldsymbol{s}_p$ refers to the scattering matrix of an idealised defect with parameter $\boldsymbol{p}$ and $\boldsymbol{n}_p$ is the distortion. Eq. (2) requires a choice as to the division between $\boldsymbol{s}_p$ and $\boldsymbol{n}_p$. The approach taken here is to choose the simplest possible model for $\boldsymbol{s}_p$ (*e.g.* a smooth defect with simple geometry) and include all other complexity in $\boldsymbol{n}_p$. This means that features such as defect roughness, material noise and many others are included in $\boldsymbol{n}_p$. In this way, $\boldsymbol{n}_p$ can be thought of as encoding all aspects that distort the measured scattering matrices from the chosen ideal scattering matrices. According to Bayes theorem [28], we have

$$P(\boldsymbol{p}|\boldsymbol{s}_n) = \frac{P(\boldsymbol{s}_n|\boldsymbol{p})P(\boldsymbol{p})}{P(\boldsymbol{s}_n)}. \tag{3}$$

Here $P(\boldsymbol{s}_n|\boldsymbol{p})$ is the probability that, for some particular distortion $\boldsymbol{n}_p$, the perturbed scattering matrix $\boldsymbol{s}_p + \boldsymbol{n}_p$ will match the experimental measurements $\boldsymbol{s}_n$. In Eq. (3), $P(\boldsymbol{p})$ is the prior probability of detecting a defect with parameter $\boldsymbol{p}$ and can in many cases be assumed to be a constant, *i.e.*, all defects are equally probable [21]. Similarly, the probability $P(\boldsymbol{s}_n)$ of experimental measurement $\boldsymbol{s}_n$ is also assumed to follow a uniform distribution over all possible measurements, which then gives

$$P(\boldsymbol{p}|\boldsymbol{s}_n) = CP(\boldsymbol{s}_n|\boldsymbol{p}). \tag{4}$$

The normalisation constant C is calculated from the condition that the total probability of a defect parameter is equal to one, $\int P(\boldsymbol{p}|\boldsymbol{s}_n)dp = 1$:

$$C = \left(\int P(\boldsymbol{s}_n|\boldsymbol{p})dp \right)^{-1}. \tag{5}$$

From Eq. (2) it follows, that the probability $P(\boldsymbol{p}|\boldsymbol{s}_n)$ can be written as

$$P(\boldsymbol{s}_n|\boldsymbol{p}) = P(\boldsymbol{s}_p + \boldsymbol{n}_p|\boldsymbol{p}) = P(\boldsymbol{n}_p|\boldsymbol{p}). \tag{6}$$

For simplicity it is assumed that the probability distribution of distortion, $P(\boldsymbol{n}_p|\boldsymbol{p})$, is independent of the defect parameter $\boldsymbol{p}$. Therefore, Eq. (6) can be further simplified as $P(\boldsymbol{s}_n|\boldsymbol{p}) = P(\boldsymbol{n}_p)$, and finally, the characterisation result is given by

$$P(\boldsymbol{p}|\boldsymbol{s}_n) = CP(\boldsymbol{n}_p). \tag{7}$$

Following Eq. (7), we can conclude that the conditional probability $P(\boldsymbol{p}|\boldsymbol{s}_n)$ of a defect parameter $\boldsymbol{p}$ given some experimental measurement $\boldsymbol{s}_n$ is determined by the probability of measuring the distortion $\boldsymbol{n}_p$. This counterintuitive result follows directly from the definition of distortion $\boldsymbol{n}_p$ adopted in this paper, and according to this definition, distortion is linked with choice of idealised scattering matrix. For the examples considered in this paper, this distortion is not solely due to noise (*e.g.* grain backscatterer) but due to a combination of other effects such as defect roughness, array element output variation, interferences from nearby defects/structural features, errors in finite element simulation and the scattering matrix extraction procedure. If backscatter is dominant and there is no interaction between the backscatter and the defect, then the distortion can be extracted from a defect-free region, but in all other cases the distortion is directly linked to the choice of idealised defects. The statistical distribution of distortion, termed the distortion model, plays a key role in defect characterisation. Based on a proper distortion model, the defect characterisation result can be obtained by calculating the conditional probability $P(\boldsymbol{p}|\boldsymbol{s}_n)$ for every possible defect parameter $\boldsymbol{p}$. It is worth pointing out that for extremely high noise cases, the scattering matrix of a small defect is negligible and we have from Eq. (2) that $\boldsymbol{n}_p = \boldsymbol{s}_n - \boldsymbol{s}_p \approx \boldsymbol{s}_n$. Hence, the distortion calculated using Eq. (2) would have little differences for different defect parameters $\boldsymbol{p}$ and the result of the characterisation procedure is a uniform distribution over all possible defect parameters. In other words, the measurement of the scattering matrix does not provide useful characterisation information in this case.

2.3. A Gaussian rough surface model of the distortion

In this section, we introduce a Gaussian rough surface model which can be used as a general form to capture different sources of coherent noise. The ideal scattering matrices of the notches shown in Fig. 1(a) can be simulated using a finite element method [29] given the width and depth values in Table 1. The distortion can then be calculated from Eq. (2), see for example, Figs. 4(a)-4(b) which show this approach applied to Notches 6 and 7. Accurate modelling of the distortion would require a large number of samples to be tested under the same measurement configuration in order to calculate the statistics of the distortion. Manufacturing many samples having the same defects as the inspected ones would require considerable time and resources, and more importantly, is only possible for ideal reference defects whose sizes and types are known. Hence, we consider using a Gaussian rough surface model of the distortion [21] in this paper, which can provide similar realisations of the distortion as in actual experiments and is easy to repeat many times to obtain different random realisations. More specifically, distortion is modelled as a two-dimensional random Gaussian rough surface [30], and the same parameters describing a Gaussian rough surface are used as parameters defining the distortion model. These parameters include the RMS roughness σ and the correlation lengths λ_1, λ_2, and given a set of parameter values, a random realisation of distortion can be obtained from [21]

$$\boldsymbol{n}_{\mathrm{gen}}(\theta_{\mathrm{in}}, \theta_{\mathrm{sc}}) = \left(\boldsymbol{c}(\theta_{\mathrm{in}}, \theta_{\mathrm{sc}}) \otimes \boldsymbol{n}_g(\theta_{\mathrm{in}}, \theta_{\mathrm{sc}}) - \mu'\right) \frac{\sigma}{\sigma'}, \tag{8}$$

where $\otimes$ is the convolution operator and μ' and σ' are mean and standard deviation of the convolution term $\boldsymbol{c} \otimes \boldsymbol{n}_g$ [31]. In addition, $\boldsymbol{n}_g$ represents uncorrelated unit variance and zero mean Gaussian white noise, and the correlation function $\boldsymbol{c}$ is given by

$$\boldsymbol{c}(\theta_{\mathrm{in}}, \theta_{\mathrm{sc}}) = \exp\left(-\frac{\varphi_1^2}{\lambda_1^2} - \frac{\varphi_2^2}{\lambda_2^2}\right), \tag{9}$$

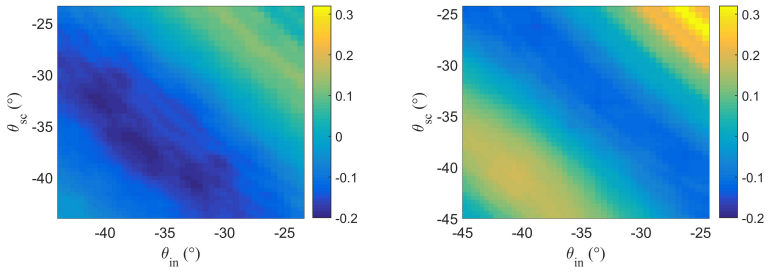

(a) (b)

Figure 4: Distortions [defined in Eq. (2)] of (a) Notch 6 and (b) Notch 7.

where an additional parameter ϕ is used to rotate the shape of the 2D correlation function such that

$$\begin{pmatrix} \varphi_1 \\ \varphi_2 \end{pmatrix} = \boldsymbol{R} \begin{pmatrix} \theta_{\text{in}} \\ \theta_{\text{sc}} \end{pmatrix}, \quad \boldsymbol{R} = \begin{pmatrix} \cos\phi & \sin\phi \\ -\sin\phi & \cos\phi \end{pmatrix}. \tag{10}$$

Figures 5(a)-5(h) show random realisations of the distortion obtained with different parameter values from Eqs. (8)-(10), where the range of the incident and scattering angles are the same as that in Fig. 3. It can be seen that parameters λ_1 and λ_2 determine the shape of the distortion and as a result, the Gaussian rough surface model can be used to simulate different types of distortion in different measurement scenarios. However, as will be discussed later, selection of the parameter values for the distortion model can, in some cases, have significant impact on the characterisation result and should be treated with care.

Since the Gaussian rough surface model enables fast simulation of different realisations of distortion, it is straightforward to calculate the statistics such as the mean and covariance matrix from the simulated data. The simulated database of distortion $\boldsymbol{N}_{\text{db}} = [\boldsymbol{n}_1, \boldsymbol{n}_2, \ldots, \boldsymbol{n}_M]$ (here $M = 1000$ is the number of the random realisations) can also be used for principal component analysis (PCA) [32] of the dataset, so that the statistics are actually calculated in a much lower dimensional space which helps to avoid the "curse of dimensionality" [33].

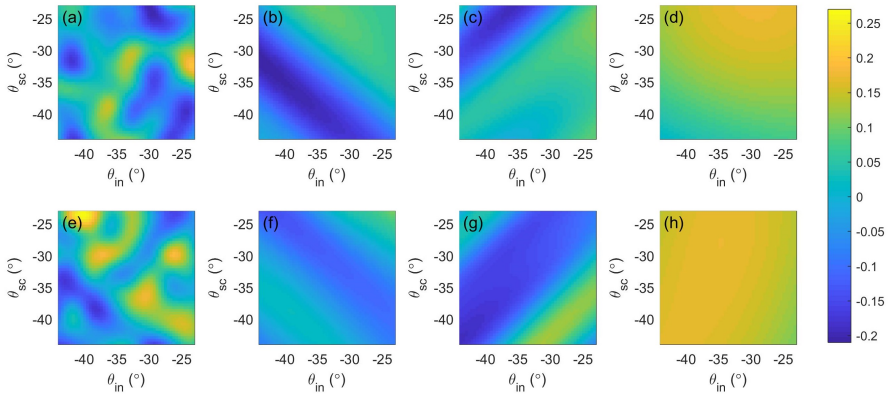

Figure 5: Random realisations of distortion obtained using the Gaussian rough surface model. (a), (e) $\lambda_1 = \lambda_2 = 2.5°$. (b), (f) $\lambda_1 = 30°, \lambda_2 = 5°$. (c), (g) $\lambda_1 = 5°, \lambda_2 = 30°$. (d), (h) $\lambda_1 = \lambda_2 = 30°$. $\sigma = 0.1$ and $\phi = -45°$ are kept the same in these figures.

The PCA process is based on eigendecomposition of the covariance matrix of the distortion database which can be expressed as

$$\boldsymbol{N}_{\text{cov}} = \boldsymbol{V}\boldsymbol{D}\boldsymbol{V}^T, \tag{11}$$

where the covariance matrix is estimated by $\boldsymbol{N}_{\text{cov}} = (\boldsymbol{N}_{\text{db}} - \boldsymbol{N}_m)(\boldsymbol{N}_{\text{db}} - \boldsymbol{N}_m)^T/(M-1)$ and the matrix $\boldsymbol{N}_m$ has the same size as $\boldsymbol{N}_{\text{db}}$ with its columns equal to the mean distortion vector $\boldsymbol{n}_m = \sum_{i=1}^{M} \boldsymbol{n}_i/M$ [21]. The column vectors of the matrix $\boldsymbol{V}$ define the axes of a new coordinate system termed the distortion PC-space, and critically, only the first few carry useful information since the corresponding eigenvalues (the diagonal elements of $\boldsymbol{D}$) are normally much larger than the rest (see Fig. 6). In the case of white Gaussian noise, the eigenvalues of the distortion database would be a constant (*i.e.* variance of the noise). However, in practice, this kind of random noise can be removed by simple averaging or filtering.

After PCA, distortion $\boldsymbol{n}$ can be transformed into the PC-space by

$$\boldsymbol{n}^{(\text{pc})} = \boldsymbol{V}^T(\boldsymbol{n} - \boldsymbol{n}_m). \tag{12}$$

It can be shown that the components of $\boldsymbol{n}^{(\text{pc})}$, corresponding to the distortion $\boldsymbol{n}$ obtained from the Gaussian rough surface model using Eq. (8), are

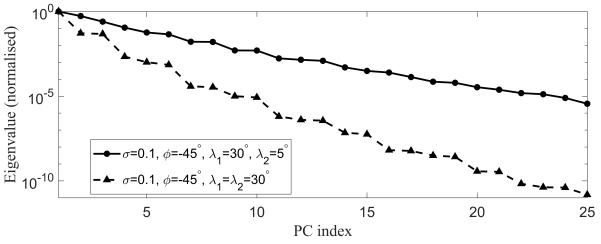

Figure 6: Normalised eigenvalues of the distortion database where the parameters of the Gaussian rough surface model are $\sigma = 0.1, \phi = -45°, \lambda_1 = 30°, \lambda_2 = 5°$ (solid line) and $\sigma = 0.1, \phi = -45°, \lambda_1 = \lambda_2 = 30°$ (dashed line).

independent in the distortion PC-space [21]. Hence, $\boldsymbol{n}^{(\mathrm{pc})}$ follows a multivariate normal distribution and the probability $P(\boldsymbol{n}^{(\mathrm{pc})})$ given the considered distortion parameters can be written as

$$P(\boldsymbol{n}^{(\mathrm{pc})}) = \frac{1}{(2\pi)^{N_s/2}|\boldsymbol{D}|^{1/2}} \exp\left(-\boldsymbol{n}^{(\mathrm{pc})T}\boldsymbol{V}\boldsymbol{D}^{-1}\boldsymbol{V}^T\boldsymbol{n}^{(\mathrm{pc})}\right), \tag{13}$$

where N_s denotes the number of components within $\boldsymbol{n}^{(\mathrm{pc})}$. Note that $\boldsymbol{n}^{(\mathrm{pc})}$ needs to be truncated (*e.g.* by using a certain threshold) in practice to prevent the result from being dominated by small eigenvalues.

The effect of the distortion model on defect characterisation is clearly seen in Eq. (13), where $\boldsymbol{V}$ and $\boldsymbol{D}$ are calculated from the distortion database $\boldsymbol{N}_{\mathrm{db}}$ through the PCA process. To select optimal parameter values for the Gaussian rough surface model, one can consider using the maximum-likelihood estimation method [21], *i.e.*:

$$[\tilde{\sigma}, \tilde{\lambda_1}, \tilde{\lambda}_2, \tilde{\phi}] = \underset{\sigma,\lambda_1,\lambda_1,\phi}{\operatorname{argmax}} \; P(\boldsymbol{n}^{(\mathrm{pc})}|\sigma, \lambda_1, \lambda_1, \phi). \tag{14}$$

In the above equation, $\boldsymbol{n}^{(\mathrm{pc})}$ is the actual distortion [*e.g.* the measurements shown in Figs. 4(a)-4(b)] in the PC-space, and the probability of measuring the distortion is calculated for different distortion models. The optimal distortion model is then selected as the set of parameters which give the maximum value for the probability $P(\boldsymbol{n}^{(\mathrm{pc})})$.

2.4. Results

For the distortion of the surface-breaking notches, the maximum-likelihood estimation process described by Eq. (14) gives suitable parameter values $\sigma = 0.1, \lambda_1 = 30°, \lambda_2 = 5°, \phi = -45°$, and hence, these values are used for characterisation in this section. The result of maximum-likelihood estimation is also seen to be reasonable if we visually compare Figs. 4(a)-4(b) to Fig. 5, since distortion obtained from the optimal parameters [Figs. 5(b), 5(f)] are clearly in better match to the experimental data than the other parameters. Note that the distortions (and scattering matrices) shown in this paper are at the array centre frequency and are estimated for discrete incident/scattering angles determined by the locations of the defect and array elements. Based on the selection of parameters for the distortion model, validation procedure for the proposed characterisation approach can be described as follows:

Step 1. Prepare the scattering matrix database for ideal reference defects.

Step 2. For each defect parameter $\boldsymbol{p}$ in the database, calculate the distortion $\boldsymbol{n}_p = \boldsymbol{s}_n - \boldsymbol{s}_p$.

Step 3. Transform distortion into the PC-space [Eq. (12)].

Step 4. Calculate the probability of measuring the distortion [Eq. (13)].

Step 5. Compare the characterisation result obtained at Step 4 with the actual defect parameter.

Figures 7(a)-7(h) show the characterisation results of Notches 1-8. The maximum characterisation errors, measured by the differences between the actual defect parameters (marked as red dots) and those corresponding to the maximum probability points, are 0.36λ (Notch 8) and 0.17λ (Notch 4) for parameters a and b. Moreover, the characterisation results of the notches are seen to have higher uncertainty in the width parameter a than the depth parameter b, and in particular, the depth results of Notches 5 and 8 are highly accurate with

small variance (*i.e.* within [1.32λ, 1.48λ] and [1.40λ, 1.50λ], while the maximum probability points correspond to the depth 1.45λ in both cases). Given the measurement configuration shown in Fig. 1(b), the measured ultrasonic array data is dominated by reflections from the vertical side of a notch facing the array, and this can explain why the depth sizing has a higher accuracy than the width sizing. The distortion model was obtained using the maximum-likelihood estimation method based on all 8 notch data and is used for calculating results for all the notches. It is suggested that this might have caused the poor width sizing for Notch 8, and the characterisation result can potentially be improved by using a different set of distortion parameters which are more suitable for Notch 8. In addition, as the defect size becomes larger, the phase part of the scattering matrix also carries important characterisation information, and this extra information can potentially be used to reduce the sizing error for Notch 8.

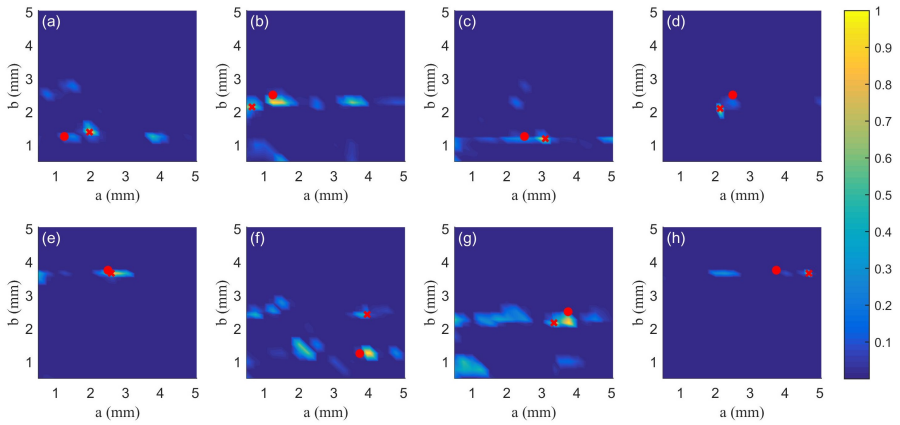

Figure 7: Characterisation results (width a and depth b) of the surface-breaking notches, where (a)-(h) are the results of Notches 1-8. The colour bar shows the normalised probability, and dots and crosses correspond to the true defect parameters and projection points on the defect manifold, respectively. Parameter values of the Gaussian rough surface model used in these results are $\sigma = 0.1, \lambda_1 = 30°, \lambda_2 = 5°$ and $\phi = -45°$.

It is worth pointing out that one of the main advantages of the characterisation method proposed in this paper is that it gives probability density

distribution of the defect parameters [21] as the characterisation result, as opposed to a fixed point in the defect parameter space that would be obtained by nearest neighbour methods. This facilitates quantification of the characterisation uncertainty, and it is desirable for real experimental measurements that are always contaminated by different sources of noise. Using the L2 norm metric, one can project the experimental data onto the defect manifold [21] to obtain the nearest point in the database. The results of this nearest neighbour approach are shown in Fig. 7 as the crosses. We find that although the projection points are close to the maximum probability points in many cases, they can also lead to large characterisation errors as shown in Fig. 7(f).

2.5. Effects of the distortion model on the characterisation performance

We have shown in Section 2.4 that characterisation results of the small surface-breaking notches are reasonably accurate by adopting the optimal distortion model. It is also important to understand the effect of different distortion models on the characterisation performance because determining the exact distortion model for an unknown defect can be difficult in practice. Figures 8(a)-8(f) show the characterisation results of Notches 6 and 7 obtained using different parameter values of the Gaussian rough surface model. The correlation lengths studied here are $\lambda_1 = \lambda_2 = 2.5^\circ$ [Figs. 8(a), 8(d)], $\lambda_1 = 5^\circ, \lambda_2 = 30^\circ$ [Figs. 8(b), 8(e)], and $\lambda_1 = \lambda_2 = 30^\circ$ [Figs. 8(c), 8(f)], and $\sigma = 0.1$ and $\phi = -45^\circ$ are kept unchanged. We can observe from Fig. 5 that none of the correlation length combinations gives similar realisations of the distortion as the actual experimental data shown in Figs. 4(a)-4(b). The results shown in Fig. 8 are thus examples of the characterisation results obtained using non-optimal distortion models. Interestingly, we find that these distortion models have produced both "accurate" [Figs. 8(c), 8(d)] and "inaccurate" [Figs. 8(a), 8(f)] characterisation results.

In order to quantitatively evaluate the characterisation performance of different distortion models, a proper distance metric is needed to compare the characterisation result $\boldsymbol{l} = [P(\boldsymbol{p}_1|\boldsymbol{s}_n), P(\boldsymbol{p}_2|\boldsymbol{s}_n), \ldots, P(\boldsymbol{p}_{N_d}|\boldsymbol{s}_n)]^T$ obtained with

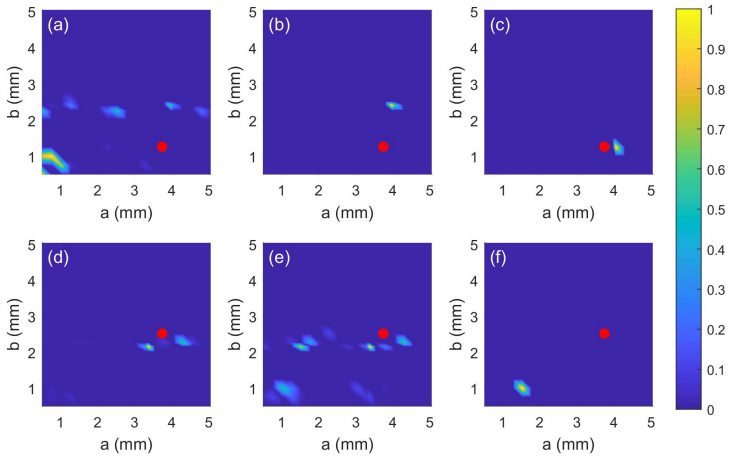

Figure 8: Characterisation results obtained with different parameter values of the Gaussian rough surface model: (a) Notch 6 with $\lambda_1 = \lambda_2 = 2.5°$, (b) Notch 6 with $\lambda_1 = 5°, \lambda_2 = 30°$, (c) Notch 6 with $\lambda_1 = \lambda_2 = 30°$, (d) Notch 7 with $\lambda_1 = \lambda_2 = 2.5°$, (e) Notch 7 with $\lambda_1 = 5°, \lambda_2 = 30°$, and (f) Notch 7 with $\lambda_1 = \lambda_2 = 30°$. The colour bar shows the normalised probability and red dots represent the true defect parameters. The same σ (= 0.1) and ϕ (= $-45°$) are used in all these results.

a certain distortion model (N_d is the number of reference defects in the database) to that obtained with the optimal distortion model (denoted as $\boldsymbol{l}_{\text{ref}}$). Here, we adopt the correlation distance for this purpose which is defined as

$$d(\boldsymbol{l}, \boldsymbol{l}_{\text{ref}}) = 1 - \rho(\boldsymbol{l}, \boldsymbol{l}_{\text{ref}}). \tag{15}$$

In the above equation, ρ is the correlation coefficient [34, 35] of two vectors:

$$\rho(\boldsymbol{l}, \boldsymbol{l}_{\text{ref}}) = \frac{\sum_{i=1}^{N_d} \left(\boldsymbol{l}(i) - \bar{l}\right) \left(\boldsymbol{l}_{\text{ref}}(i) - \bar{l}_{\text{ref}}\right)}{\sqrt{\left(\sum_{i=1}^{N_d} (\boldsymbol{l}(i) - \bar{l})^2\right) \left(\sum_{i=1}^{N_d} (\boldsymbol{l}_{\text{ref}}(i) - \bar{l}_{\text{ref}})^2\right)}}, \tag{16}$$

where $\bar{l} = \bar{l}_{\text{ref}} = 1/N_d$ are mean values of the vectors $\boldsymbol{l}$ and $\boldsymbol{l}_{\text{ref}}$. Although the correlation lengths $\lambda_1 = \lambda_2 = 30°$ have produced "accurate" characterisation result for Notch 6 as shown in Fig. 8(c), it is noted that the characterisation uncertainty is indeed underestimated and hence, characterisation results obtained using the same distortion model can potentially have large errors in some cases [see Fig. 8(f)]. The correlation distance defined in Eq. (15) quantifies the

amount of deviation from $\boldsymbol{l}_{\text{ref}}$ for a characterisation result $\boldsymbol{l}$ (smaller values indicate better matches to $\boldsymbol{l}_{\text{ref}}$), and the distance values are 0.81 (caused by a large characterisation error), 0.76 (caused by a large characterisation error), and 0.49 (caused by an underestimation of the characterisation uncertainty) for the results shown in Figs. 8(a)-8(c), respectively. For the results of Notch 7 [Figs. 8(d)-8(f)], the correlation distance is calculated as 0.45 (caused by an underestimation of the characterisation uncertainty), 0.47 (caused by the discrepancy in the characterisation uncertainty compared to $\boldsymbol{l}_{\text{ref}}$), and 1.01 (indicating a large characterisation error).

The characterisation performance of different distortion models is further investigated and Figs. 9(a)-9(b) show the distance maps (*i.e.* correlation distances of different distortion models) for Notches 6 and 7. In Figs. 9(a)-9(b), the top and bottom rows correspond to $\phi = 0°$ and $\phi = -45°$, and each column represents a fixed value of σ between 0.05 and 0.2. It can be seen that there exist areas where the correlation distance is large (*e.g.* over 0.7) in both cases, indicating poor characterisation results. We also find that the effect of σ and λ_1 is relatively small as long as near-optimal values of λ_2 and ϕ are used (see red boxes in Fig. 9 which highlight regions where the characterisation results are most desirable). It is worth emphasizing that the effect of distortion models on characterisation depends on the measurement configuration, sources of experimental noise and size/type of a defect. The same distortion model can potentially have significantly different characterisation performance in different measurement scenarios, and this issue is further explored in the next section.

3. Robust defect characterisation and experimental results of real defects

We aim to characterise more realistic defects having irregular shapes in this section. The studied defects have small sizes (less than 2λ) and can be detected from an image, and as in the case of practical inspection scenarios, the actual defect geometry (and thus the idealised scattering matrix) is unknown. One

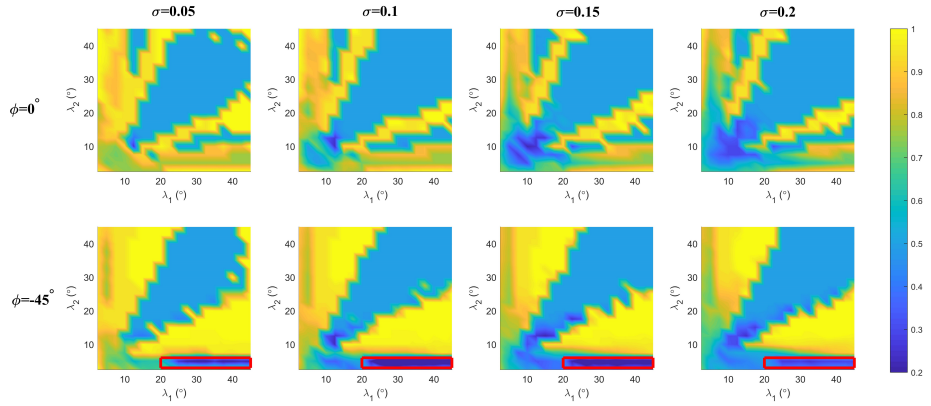

(a)

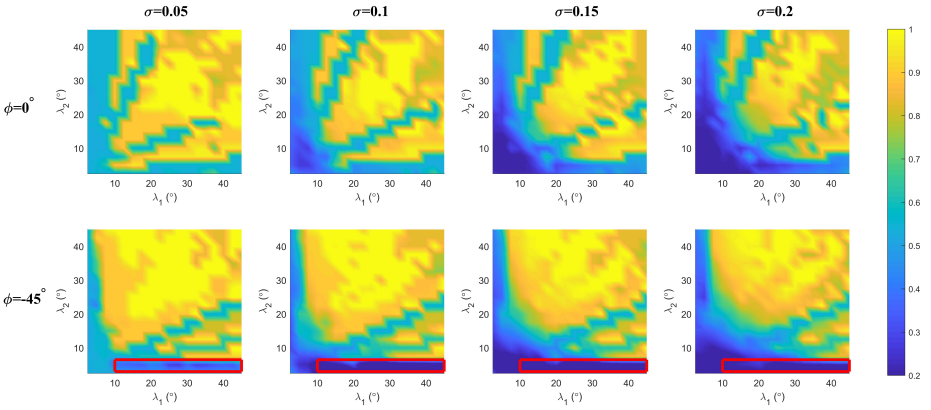

(b)

Figure 9: Distance maps showing the correlation distances [see Eq. (15)] between the characterisation results obtained with different distortion models and those obtained with the optimal distortion model for (a) Notch 6 and (b) Notch 7. In both results, the top and bottom rows correspond to $\phi = 0°$ and $\phi = -45°$, respectively, and each column represents a fixed value of σ between 0.05 and 0.2. Red boxes show regions where the parameters λ_2 and ϕ are near-optimal.

of the main advantages of the defect characterisation approach introduced in Section 2.2 is that it can be applied to different types of defects as long as the defect geometry is described by a small number of parameters such as size,

orientation angle and aspect ratio. To illustrate this, we selected fatigue cracks [Fig. 10(a)] and volumetric defects in an additive manufactured (AM) sample [Fig. 10(b)] to evaluate the performance of the characterisation approach on real defects. In Fig. 10(a), the fatigue crack was grown from an EDM starter notch in a fatigue testing machine (Instron 8801) under 3-point bending tests [22]. Six specimens with cracks of varying sizes were manufactured and measurements were performed on these specimens using a 2.5 MHz, 64 element array with an element pitch of 0.5mm (the EDM starter notches were removed by machining a layer away before array measurements). The same measurement configuration as in Fig. 1(b) was adopted except that the distance between the crack and array is now approximately 35mm [see Fig. 11(a) for TFM image of one of the cracks]. The sample shown in Fig. 10(b) was built using a Realiser SLM50 from Aluminium powder feedstock, with standard Realiser 10mm Aluminium build plate. The built was $40\times20\times10$ mm^3. The built design included six side through holes. The holes were designed to replicate cylindrical side drilled holes, while having similar characteristics to defects found within PBF components, such as internal surface roughness and backfilling. The smaller defects (designed to be 0.5mm in diameter) were chosen to replicate the same order of magnitude found in classic PBF defects. The larger defects (designed to be 1mm in diameter) were chosen to replicate small features commonly manufactured using processes such as PBF. The holes were equally spaced at increments of 5mm horizontally. The shallowest hole was placed 6mm from the base of the build and the defects following that were placed at depths increasing by 2mm per hole. A 10 MHz, 128 element array (element pitch: 0.3mm) was attached to the top of the 10mm built plate to measure the FMC data of the defects, and Fig. 11(b) shows the TFM image of the AM sample.

Both the TFM results in Fig. 11 confirm the need for scattering-matrix-based characterisation as it is difficult to determine the sizes/types of the defects from these images. We note that determination of the optimal distortion model cannot be carried out as in the previous section because the idealised defect scattering matrix is unknown. In order to fully consider all possible distortion

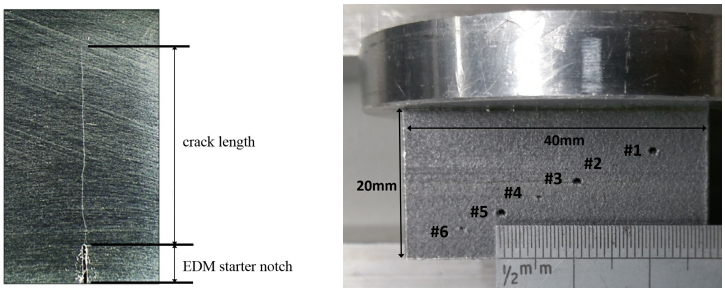

(a) (b)

Figure 10: (a) An Aluminium sample containing a fatigue crack grown under 3-point bending tests [22], and (b) additive manufactured (AM) Aluminium specimen containing six volumetric defects [23]. In (b), the array was attached to the build plate (top) which has a smooth surface.

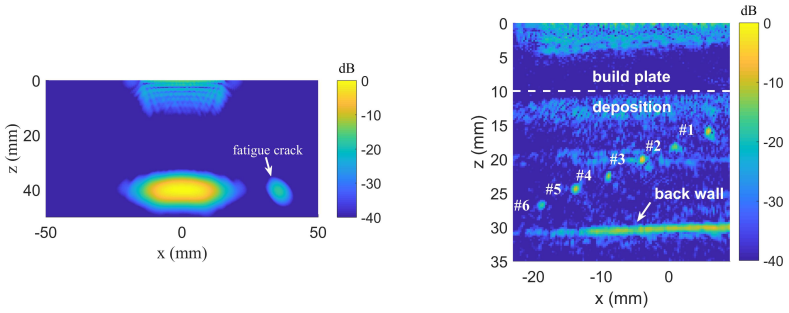

(a) (b)

Figure 11: TFM images of: (a) a small fatigue crack, and (b) volumetric defects in the AM specimen. The size of the crack in (a) was determined as 2mm from TFM result in a previous study using a 10 MHz array [22]. In (b), the design sizes of Defects 1, 3, and 5 are 1mm, and those of Defects 2, 4, and 6 are 0.5mm.

models given an experimental data $\boldsymbol{s}_n$, it is proposed here that the final result can be taken as the weighted sum of the characterisation results obtained with different distortion models as

$$
\begin{aligned}
P_{\text{avg}}(\boldsymbol{p}_0|\boldsymbol{s}_n) &= \sum P(\sigma,\lambda_1,\lambda_2,\phi)P(\boldsymbol{p}_0|\boldsymbol{s}_n;\sigma,\lambda_1,\lambda_2,\phi) \\
&= \sum P(\sigma,\lambda_1,\lambda_2,\phi)C(\sigma,\lambda_1,\lambda_2,\phi)P(\boldsymbol{s}_n-\boldsymbol{s}_0;\sigma,\lambda_1,\lambda_2,\phi) \qquad (17)\\
&= \sum P(\sigma,\lambda_1,\lambda_2,\phi)C(\sigma,\lambda_1,\lambda_2,\phi)P(\boldsymbol{n}_{p0}^{(\text{pc})};\sigma,\lambda_1,\lambda_2,\phi),
\end{aligned}
$$

where $P(\sigma,\lambda_1,\lambda_2,\phi)$ denotes the prior probability of a distortion model and is assumed to be a constant for a specific experimental configuration. The last term $P(\boldsymbol{n}_{p0}^{(\text{pc})};\sigma,\lambda_1,\lambda_2,\phi)$ of Eq. (17) is the same as in Eq. (13) and the normalisation constants $C(\sigma,\lambda_1,\lambda_2,\phi)$ can be determined for individual distortion models separately using Eq. (5).

We term the characterisation approach described above robust defect characterisation, because it can avoid poor characterisation results caused by inaccurate assumptions about the distortion and produce more reliable defect characterisation. For characterisation of the fatigue cracks, because the measurement configuration including the array and the inspection material are the same as those used for the machined notches in Section 2.1, we fixed the RMS value σ and rotation angle ϕ to be 0.1 and $-45°$, respectively. From Figs. 5(d), 5(h), we find that distortion models with large correlation lengths represent near-constant errors among all the transmit-receive channels and thus indicate a systematic error in the array measurement system. On the other hand, as the correlation lengths λ_1 and λ_2 converge to 0 [see for example, Figs. 5(a), 5(e) where $\lambda_1 = \lambda_2 = 2.5°$], the resultant distortion becomes incoherent with the defect scattering matrix and is easy to remove. The range of the correlation lengths used for characterisation is chosen to be between 5° and 30° based on the above considerations. For the AM specimen, we also varied the RMS value σ between 0.15 and 0.3 as measurements were taken at a higher frequency.

The characterisation results of the fatigue cracks calculated using Eq. (17) are shown in Fig. 12 (the angle of a surface-breaking crack is defined with respect to the backwall normal direction and is positive if measured clockwise). The dashed lines correspond to crack sizes measured from TFM images (*i.e.* the distances between the crack tip and mouth indications) using a 10 MHz

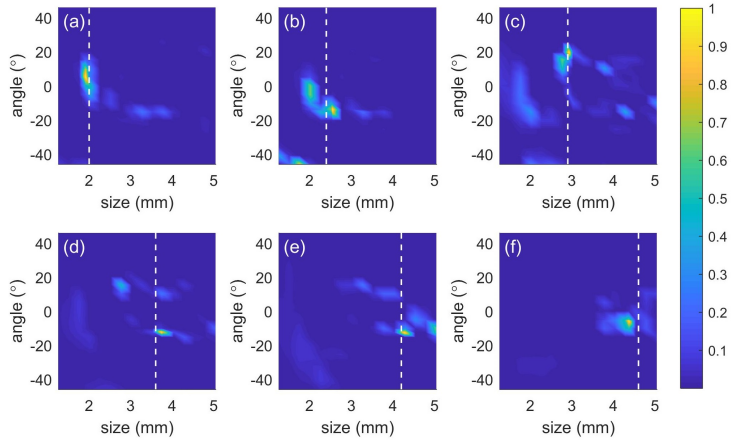

Figure 12: Characterisation results of the fatigue cracks using scattering matrices measured at 2.5 MHz. The colour bar shows the normalised probability, and dashed lines represent crack sizes measured from TFM images at 10 MHz [22].

array in a previous study [22]. It can be seen that although the results of the fatigue cracks have a degree of uncertainty, the maximum probability point is close to the dashed line in all the cases and the maximum sizing error is 0.09λ or 0.23mm [Fig. 12(f)]. These results also show that the fatigue cracks have relatively small orientation angles [less than 15° except the result in Fig. 12(c)]. This suggests that the crack growth directions from the EDM notches were near vertical under the 3-point bending tests, and it is in good agreement with the optical image of the crack shown in Fig. 10(a).

Figures 13(a)-13(f) show the characterisation results of Defects 1-6 in the AM sample. Besides size, aspect ratio is selected as the second defect parameter which quantifies the width of an elliptical defect (*e.g.* 0 for an ideal crack and 1 for a side-drilled hole). The red dots in these results correspond to the average defect size and aspect ratio, and they are calculated from 231 cross section images of the defects which are obtained from X-ray CT data (histogram plots of the size and aspect ratio distribution can be found in the supplemental material). It can be seen that accurate sizing has been achieved using the proposed robust defect characterisation approach, and errors are within 0.09mm (0.15λ)

except for Defect 5 [Fig. 13(e)]. However, the aspect ratio results consistently show high uncertainty, and in particular, the probability of the defect being crack-like is high for the smaller defects [Figs. 13(b), 13(d), and 13(f)]. Hence, these results show that defect type classification is fundamentally challenging for defects whose sizes are only comparable to half a wavelength. The maximum probability points give aspect ratio values near 0.5 for the larger defects [Figs. 13(a), 13(c), and 13(e)] and their widths are thus underestimated. The actual defect parameter points (red dots) do fall within the shown probability distributions, and it demonstrates the robustness of our method. It is worth pointing out that the defect model (*i.e.* scattering matrix database) is too simplistic in this case because defect geometry (see the supplemental material) cannot be adequately described by an ellipse with two parameters. Moreover, it is noted that the simple averaging of the characterisation results (*i.e.* all distortion models considered are equally probable) is a potential cause for the inaccuracy in the width sizing of the larger defects. The use of more precise distortion models, tailored to the rough shapes of the manufactured defects, is expected to improve the characterisation accuracy.

Table 2: Summary statistics of the correlation distances of individual distortion models used for characterisation of the fatigue cracks. Here, length refers to the crack size determined from TFM images at 10 MHz [22].

Length (mm)	Mean	Standard deviation	Minimum	Maximum
2.0	0.11	0.07	0.02	0.34
2.4	0.05	0.03	0.01	0.19
2.9	0.22	0.11	0.08	0.51
3.6	0.14	0.10	0.03	0.47
4.2	0.29	0.20	0.05	0.75
4.6	0.26	0.17	0.04	0.74

Summary statistics of the correlation distance values of individual distortion models are given in Tables 2 and 3, respectively, for characterisation of the fatigue cracks and defects in the AM sample. Note that for these real defects,

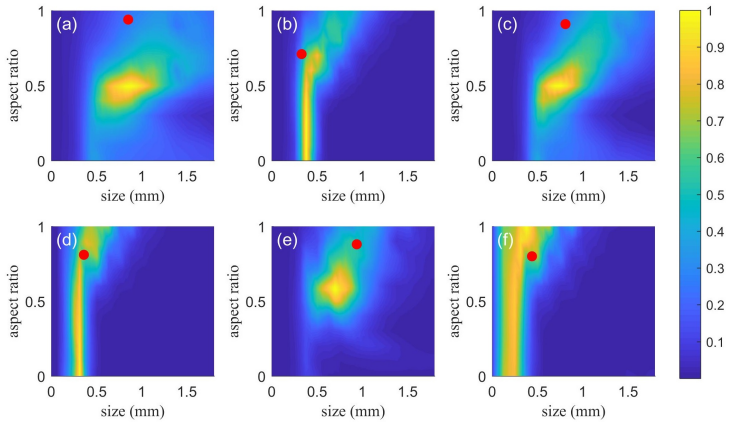

Figure 13: Characterisation results of the volumetric defects shown in Fig. 10(b) using scattering matrices measured at 10 MHz. The colour bar shows the normalised probability, and the red dots represent average defect size and aspect ratio values extracted from X-ray CT data.

Table 3: Summary statistics of the correlation distances of individual distortion models used for characterisation of the defects in the AM sample.

Defect	Mean	Standard deviation	Minimum	Maximum
1	0.27	0.16	0.04	0.98
2	0.05	0.03	0.01	0.17
3	0.19	0.13	0.03	0.67
4	0.05	0.05	3.5×10^{-3}	0.25
5	0.07	0.06	4.9×10^{-3}	0.26
6	0.19	0.15	0.02	0.80

the optimal result $\boldsymbol{l}_{\text{ref}}$ in Eq. (15) is replaced by $\boldsymbol{l}_{\text{avg}}$ which represents the output of robust defect characterisation [see Eq. (17)]. We can see that correlation distances of the individual distortion models are in general lower than those shown in Fig. 9, because characterisation results of all distortion models have contributed to the result $\boldsymbol{l}_{\text{avg}}$. However, we still find large correlation distances (over 0.7) for fatigue cracks of sizes 4.2mm and 4.6mm, suggesting that the characterisation result is indeed very poor in certain cases. Because we varied

the value of σ (between 0.15 and 0.3) when characterising defects in the AM sample, larger correlation distance values are found in Table 3. However, the mean correlation distance is consistently small, so the contribution from very "poor" distortion models to the final result is relatively small.

4. Conclusions

A robust defect characterisation approach is proposed in this paper which can be implemented in a fully automated way. This approach is based on the finding that the conditional probability of a defect parameter given some measurement is proportional to the probability of observing the "distortion", defined as the difference between the experimentally measured scattering matrix and its idealised counterpart(s). Following this definition, distortion is linked to the choice of the reference defects in the database and it encodes all the aspects that can potentially affect accurate measurement of a scattering matrix. The Gaussian rough surface model of the distortion with parameters σ (RMS amplitude), λ_1 and λ_2 (correlation lengths), and ϕ (the rotation angle) is suitable to model different types of distortion by using different parameter values. It is shown through experiments that optimal parameters of the Gaussian rough surface model can be obtained by adopting a maximum-likelihood estimation method for idealised defects.

The true defect geometry is unknown in practice and the robust defect characterisation approach calculates the weighted sum of the results obtained with different distortion models. This is particularly desirable for inspection of AM specimens as there exist a wide variety of "natural" defects (*i.e.* sources of distortion) which are introduced during the manufacturing process. Robust defect characterisation is shown to perform reliably by characterising volumetric defects in an AM sample and real fatigue cracks. The relatively long processing time (needed to compute results for multiple distortion models) is one of the main limitations of this approach, but this can potentially be overcome by using parallel processing. It is possible to introduce additional defect parameters

which describe the detailed defect geometry in order to consider multiple defect types. On one hand, our approach is generalisable to higher defect parameter spaces because of the analytic expression for the probability shown in Eq. (13), *i.e.*, calculating the conditional probability of a defect parameter simply requires an evaluation of the probability density of a multivariate Gaussian function at a given point. On the other hand, as the number of idealised defects increases exponentially with the increase of the dimensionality of the defect database, we note that there is a trade-off between the computational burden of the approach and the achievable characterisation performance. Future work will aim to establish more accurate prior distribution for different distortion models which can help avoid underestimation/overestimation of the characterisation uncertainty.

Acknowledgement

The project leading to this application has received funding from the European Unions Horizon 2020 research and innovation programme under grant agreement No. 755500, and the Engineering and Physical Sciences Research Council (UK, EPSRC) under Grant No. EP/L022125/1.

References

[1] J. D. Achenbach, Quantitative nondestructive evaluation, Int. J. Solids Struct. 37 (1-C2) (2000) 13–27. doi:10.1016/S0020-7683(99)00074-8.

[2] P. Calmon, A. Lhémery, I. Lecœur-Taïbi, R. Raillon, L. Paradis, Models for the computation of ultrasonic fields and their interaction with defects in realistic NDT configurations, Nucl. Eng. Des. 180 (3) (1998) 271–283. doi:10.1016/S0029-5493(97)00299-9.

[3] O. Zahran, W. Al-Nuaimy, Automatic segmentation of time-of-flight diffraction images using time-frequency techniques application to rail-track defect detection, Insight 46 (6) (2004) 338–343. doi:10.1784/insi.46.6.338.56384.

[4] G. P. Gunarathne, R. W. Keatch, Novel techniques for monitoring and enhancing dissolution of mineral deposits in petroleum pipelines, Ultrasonics 34 (2–5) (1996) 411–419. doi:10.1016/0041-624X(96)00016-9.

[5] B. Shakibi, F. Honarvar, M. D. Moles, J. Caldwell, A. N. Sinclair, Resolution enhancement of ultrasonic defect signals for crack sizing, NDT E Int. 52 (2012) 37–50. doi:10.1016/j.ndteint.2012.08.003.

[6] S. P. Kelly, R. Farlow, G. Hayward, Applications of through-air ultrasound for rapid NDE scanning in the aerospace industry, IEEE Trans. Ultrason. Ferroelectr. Freq. Control 43 (4) (1996) 581–591. doi:10.1109/58.503780.

[7] D. Robinson, Identification and sizing of defects in metallic pipes by remote field eddy current inspection, Tunn. Undergr. Sp. Tech. 13 (1998) 17–27. doi:10.1016/S0886-7798(98)00090-X.

[8] B. W. Drinkwater, P. D. Wilcox, Ultrasonic arrays for non-destructive evaluation: A review, NDT E Int. 39 (7) (2006) 525–541. doi:10.1016/j.ndteint.2006.03.006.

[9] C. Holmes, B. W. Drinkwater, P. D. Wilcox, Post-processing of the full matrix of ultrasonic transmit-receive array data for nondestructive evaluation, NDT E Int. 38 (8) (2005) 701–711. doi:10.1016/j.ndteint.2005.04.002.

[10] L. Le Jeune, S. Robert, E. L. Villaverde, C. Prada, Plane wave imaging for ultrasonic non-destructive testing: Generalization to multimodal imaging, Ultrasonics 64 (2016) 128–138. doi:10.1016/j.ultras.2015.08.008.

[11] G. Montaldo, M. Tanter, J. Bercoff, N. Benech, M. Fink, Coherent plane-wave compounding for very high frame rate ultrasonography and transient elastography, IEEE Trans. Ultrason. Ferroelectr. Freq. Control 56 (3) (2009) 489–506. doi:10.1109/TUFFC.2009.1067.

[12] C. Prada, S. Manneville, D. Spoliansky, M. Fink, Decomposition of the time reversal operator: Detection and selective focusing on two scatterers, J. Acoust. Soc. Am. 99 (4) (1996) 2067–2076. doi:10.1121/1.415393.

[13] S. Shahjahan, A. Aubry, F. Rupin, B. Chassignole, A. Derode, A random matrix approach to detect defects in a strongly scattering polycrystal: How the memory effect can help overcome multiple scattering, Appl. Phys. Lett. 104 (23) (2014) 234105. doi:10.1063/1.4882421.

[14] L. Lin, H. Cao, Z. Luo, Total focusing method imaging of multidirectional CFRP laminate with model-based time delay correction, NDT E Int. 97 (2018) 51–58. doi:10.1016/j.ndteint.2018.03.011.

[15] J. Blitz, G. Simpson, Ultrasonic methods of non-destructive testing, Chapman & Hall, London, UK, 1996.

[16] British Standards Institution, Non-destructive testing - Ultrasonic testing - Characterisation and sizing of discontinuities, BS EN ISO 16827, London, UK, 2014.

[17] ASTM International, Standard practice for contact ultrasonic testing of welds using phased arrays, ASTM E2700-14, West Conshohocken, PA, 2014.

[18] J. Zhang, B. W. Drinkwater, P. D. Wilcox, The use of ultrasonic arrays to characterize crack-like defects, J. Nondestruct. Eval. 29 (4) (2010) 222–232. doi:10.1007/s10921-010-0080-6.

[19] X. Li, Y. Wang, P. Ni, H. Hu, Y. Song, Flaw sizing using ultrasonic C-scan imaging with dynamic thresholds, Insight 59 (11) (2017) 603–608. doi:10.1784/insi.2017.59.11.603.

[20] J. Zhang, B. W. Drinkwater, P. D. Wilcox, Defect characterization using an ultrasonic array to measure the scattering coefficient matrix, IEEE Trans. Ultrason. Ferroelectr. Freq. Control 55 (10) (2008) 2254–2265. doi:10.1109/TUFFC.924.

[21] A. Velichko, L. Bai, B. W. Drinkwater, Ultrasonic defect characterization using parametric-manifold mapping, Proc. R. Soc. A 473 (2202) (2017) 20170056. doi:10.1098/rspa.2017.0056.

[22] C. Peng, L. Bai, J. Zhang, B. W. Drinkwater, The sizing of small surface-breaking fatigue cracks using ultrasonic arrays, NDT E Int. 99 (2018) 64–71. doi:10.1016/j.ndteint.2018.06.005.

[23] T. Stratoudaki, Y. Javadi, W. Kerr, P. D. Wilcox, D. Pieris, M. Clark, Laser induced phased arrays for remote ultrasonic imaging of additive manufactured components, in: 57th Annual Conference of the British Institute of Non-Destructive Testing, NDT 2018, 2018, pp. 174–182.

[24] S. K. Everton, M. Hirsch, P. Stravroulakis, R. K. Leach, A. T. Clare, Review of in-situ process monitoring and in-situ metrology for metal additive manufacturing, Mater. Design 95 (2016) 431–445. doi:10.1016/j.matdes.2016.01.099.

[25] N. T. Aboulkhair, N. M. Everitt, I. Ashcroft, C. Tuck, Reducing porosity in AlSi10Mg parts processed by selective laser melting, Addit. Manuf. 1 (2014) 77–86. doi:10.1016/j.addma.2014.08.001.

[26] A. Velichko, P. D. Wilcox, Reversible back-propagation imaging algorithm for postprocessing of ultrasonic array data, IEEE Trans. Ultrason. Ferroelectr. Freq. Control 56 (11) (2009) 2492–2503. doi:10.1109/TUFFC.2009.1336.

[27] L. Bai, A. Velichko, B. W. Drinkwater, Ultrasonic defect characterisation - Use of amplitude, phase, and frequency information, J. Acoust. Soc. Am. 143 (1) (2018) 349–360. doi:10.1121/1.5021246.

[28] T. Hastie, R. Tibshirani, J. Friedman, The elements of statistical learning, 2nd Edition, Springer-Verlag, New York, NY, 2009.

[29] A. Velichko, P. D. Wilcox, A generalized approach for efficient finite element modeling of elastodynamic scattering in two and three dimensions, J. Acoust. Soc. Am. 128 (3) (2010) 1004–1014. doi:10.1121/1.3467775.

[30] F. Shi, W. Choi, M. J. Lowe, E. A. Skelton, R. V. Craster, The validity of kirchhoff theory for scattering of elastic waves from rough surfaces, Proc. R. Soc. A 471 (2178) (2015) 20140977. doi:10.1098/rspa.2014.0977.

[31] D. J. Whitehouse, Surface characterization and roughness measurement in engineering, in: Photomechanics, Springer, Berlin, Heidelberg, 2000, pp. 413–461.

[32] I. T. Jolliffe, Principal component analysis, 2nd Edition, Springer-Verlag, New York, NY, 2002.

[33] R. E. Bellman, Adaptive control processes: A Guided Tour, Princeton Univ. Press, Princeton, NJ, 1961.

[34] K. Pearson, Contributions to the mathematical theory of evolution-iii. regression, heredity, and panmixia, Philos. Trans. R. Soc. Lond. A 187 (1896) 253–318.

[35] L. Bai, A. Velichko, B. W. Drinkwater, Ultrasonic characterization of crack-like defects using scattering matrix similarity metrics, IEEE Trans. Ultrason. Ferroelectr. Freq. Control 62 (3) (2015) 545–559. doi:10.1109/TUFFC.2014.006848.